

## Electronic Supplementary Information (ESI)

3D Printing of Highly Textured Bulk Thermoelectric Materials:

Mechanically Robust BiSbTe Alloys with Superior Performance

Junhao Qiu<sup>1</sup>, Yonggao Yan<sup>1\*</sup>, Tingting Luo<sup>1</sup>, Kechen Tang<sup>1</sup>, Lei Yao<sup>1</sup>, Jian Zhang<sup>1</sup>, Min Zhang<sup>1</sup>, Xianli Su<sup>1</sup>, Gangjian Tan<sup>1</sup>, Hongyao Xie<sup>2</sup>, Mercouri G Kanatzidis<sup>2</sup>, Ctirad Uher<sup>3\*</sup>,  
Xinfeng Tang<sup>1\*</sup>

*1, State Key Laboratory of Advanced Technology for Materials Synthesis and Processing, Wuhan University of Technology, Wuhan, Hubei 430070, China*

*2, Department of Chemistry, University of Northwestern, Evanston, Illinois 60208, United States*

*3, Department of Physics, University of Michigan, Ann Arbor, Michigan 48109, United States*

*\*Corresponding authors: Y. Yan (yanyonggao@whut.edu.cn), C. Uher (cuher@umich.edu),*

*X. Tang (tangxf@whut.edu.cn).*

**Microstructure of p-type BiSbTe material prepared by thermal explosion**

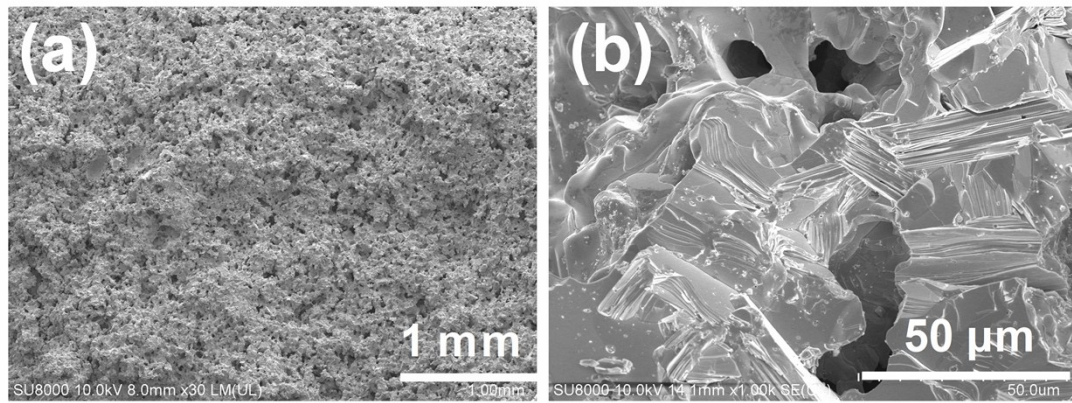


**Figure S1.** SEM images of  $\text{Bi}_{0.4}\text{Sb}_{1.6}\text{Te}_3$  product prepared by thermal explosion.

## Powder properties

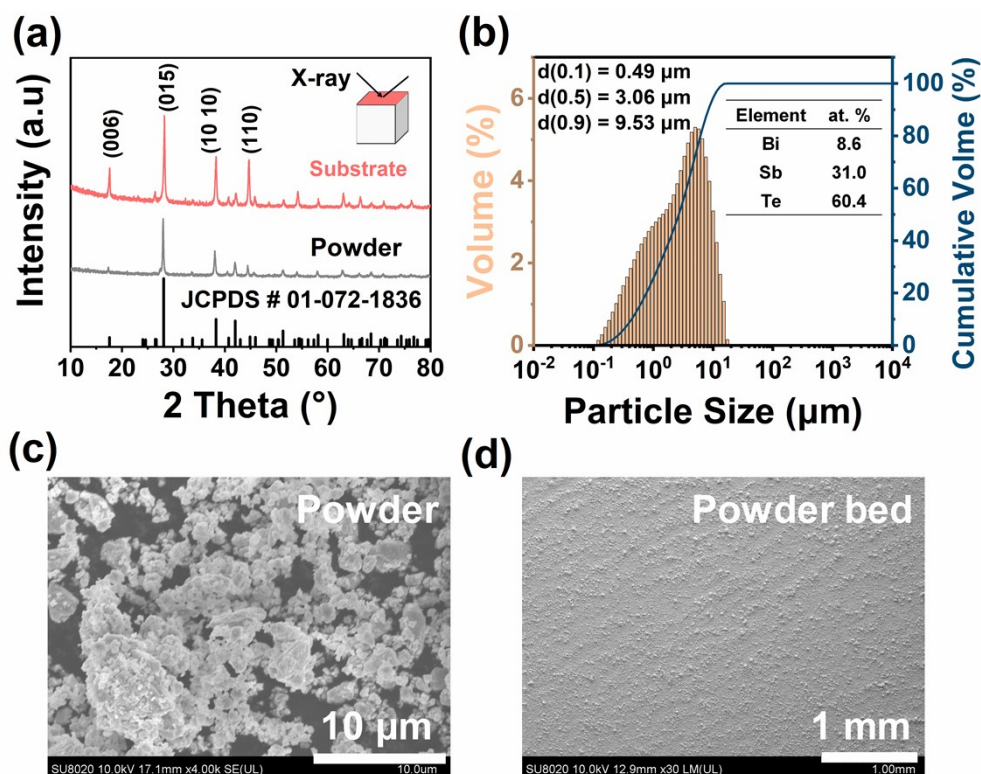


**Figure S2.** Powder properties. (a) XRD patterns of the p-type BiSbTe powder prepared by thermal explosion and of a substrate densified by SPS; (b) Powder precursor size and its distribution, with the inset showing the chemical composition of the powder; (c) the powder precursor particle morphology after 400 mesh sieving; (d) surface morphology of the powder bed after being quickly dried.

As depicted in Figure S2 (a), XRD patterns of the precursor powder and of the substrate are completely consistent with standard  $\text{Bi}_{0.4}\text{Sb}_{1.6}\text{Te}_3$  diffraction peaks in the range of the diffraction angle with no other diffraction peaks that might indicate the presence of secondary phases. Thus, the prepared powder and substrate are single phase structures. Besides, it shows that the substrate fabricated by SPS is polycrystalline with no evidence of preferential orientation since the relative intensities of different peaks almost correspond to that of the standard powder sample. Figure S2 (b) shows the distribution of particle sizes in the precursor powder. The average size of particles in the powder is 3.06 μm and more than 90% of the particles have sizes below 10 μm. The inset shows the actual chemical composition of the powder. The composition is almost consistent with the

nominal composition, demonstrating that p-type BiSbTe precursor powders with controllable compositions and uniform sizes can be obtained by thermal explosion combined with ball milling. The powder's properties are suitable to be used as powder beds. Although the particles of the powder have irregular shapes and a small amount of them have already agglomerated, as shown in Figure S2 (c), the agglomerated particles become completely dispersed upon enhancing the fluidity of the powder by dispersing it in ethanol to make a slurry. The surface morphology of the powder bed after being quickly dried is flat, uniform and compact, as shown in Figure S2 (d).

## ANSYS simulation

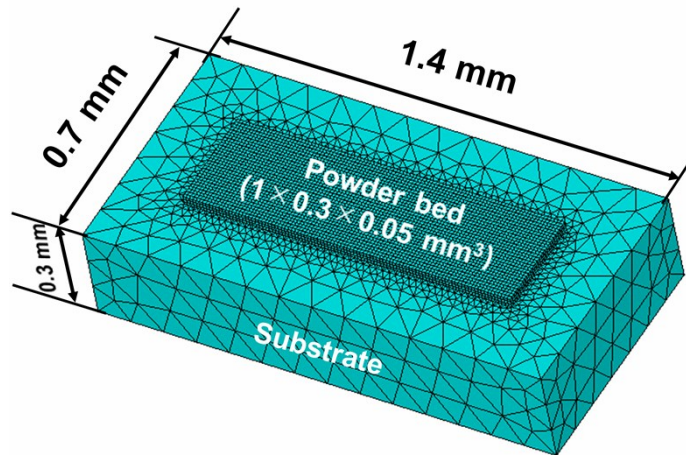


**Figure S3.** Three-dimensional finite element model of the powder bed and substrate.

**Table S1.** The as-used SLM processing conditions in the ANSYS simulation calculation

Parameter	Value
Laser absorptivity	0.3
Ambient temperature, K	298
Laser wavelength, nm	1064
Radius of laser beam, $\mu\text{m}$	50
Laser power, W	7
Scanning speed, m/s	200
Hatch space, nm	50
Number of scans	2
Size of power bed, mm	1×0.3×0.05 (length × width × thickness)
Melting point, K	893
Boiling point, K	1837

## Thin layer forming

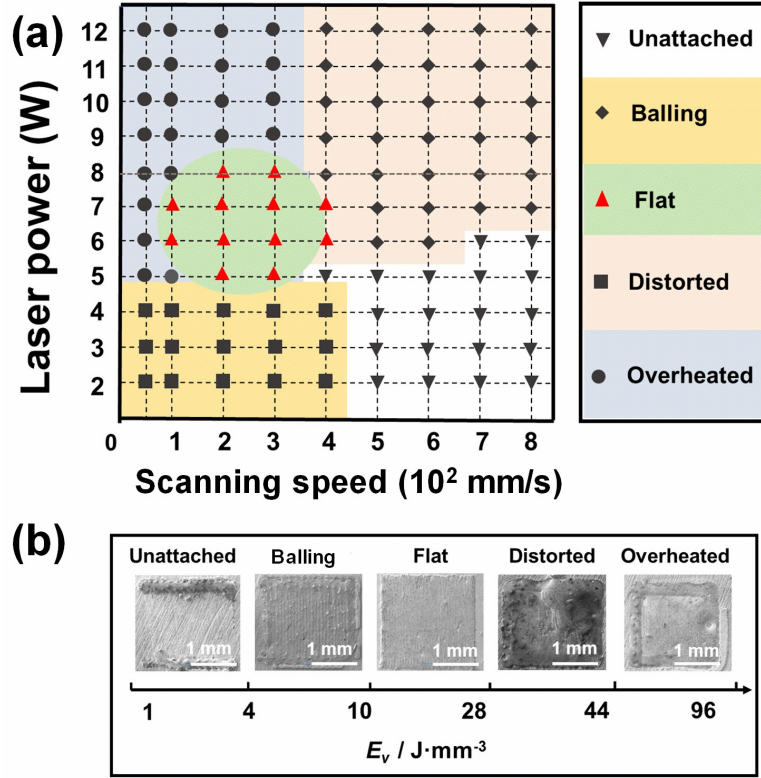


**Figure S4.** (a) Process window for forming a thin-layer at different laser power and scanning speed, the five different color regions represent five typical surface morphologies of the forming thin-layer, respectively; (b) the Semi-quantitative relationship between the energy volume density ( $E_v$ ) and the surface morphologies of the forming layers.

The SLM process involves many processing parameters (laser power, scanning speed, hatch spacing, thickness of powder bed, etc.), the interaction of these parameters jointly determines the microstructure and composition of the SLM samples. To comprehensively and quantitatively understand the effects of these processing parameters on the forming quality of the powder bed, the above parameters can be integrated into the parameter of laser volume energy density ( $E_v$ ,  $J \cdot mm^{-3}$ ) defined as<sup>1</sup>:

$$E_v = \frac{P}{v d h} \quad (1)$$

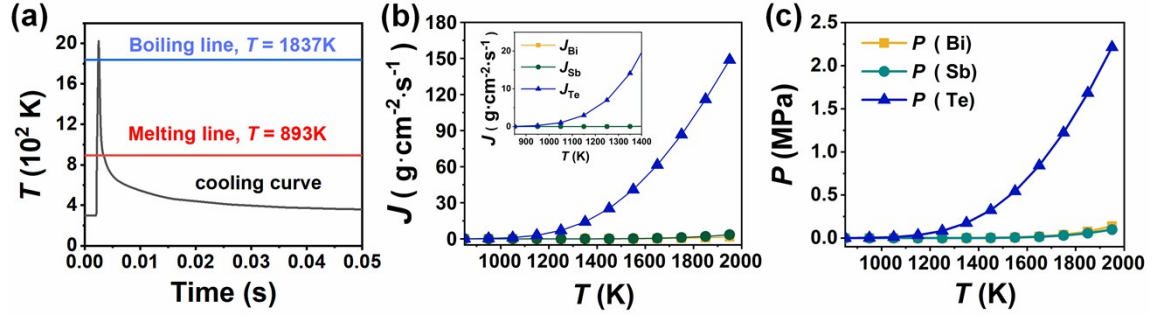
where  $P$ ,  $v$ ,  $d$  and  $h$  are the laser power (W), scanning speed ( $mm \cdot s^{-1}$ ), powder bed thickness (mm), and hatch spacing (mm), respectively.

Figure S4 (a) presents the process window for forming a thin-layer with area  $2 \times 2 \text{ mm}^2$  under

different laser power ( $P = 2\text{-}12\text{ W}$ ) and scanning speed ( $v = 25\text{-}800\text{ mm s}^{-1}$ ). According to the surface morphology characteristics of the forming layers, five typical surface morphologies can be distinguished and categorized as unattached, balling, flat, distorted and overheated, respectively. The relationship between the above morphologies and the laser power and scanning speed can be marked by five different colors, as shown in Figure S4 (a). Figure S4 (b) presents the semi-quantitative relationship between the volume energy density  $E_v$  and the characteristic morphology of the forming thin layer. When  $E_v$  is large enough ( $44\text{ J mm}^{-3} < E_v < 96\text{ J mm}^{-3}$ ), the energy absorbed by the powder bed is much larger than its melting threshold, and this results in the molten pool's temperature being too high. The viscosity thus decreases, the Marangoni convection inside the molten pool increases, the liquid flow rate intensifies, and the neighboring unirradiated powder is also being melted. Under these conditions, the temperature of the molten pool reaches rather high levels, the low viscosity greatly contributes to melt flowing and, finally, the boundary of the forming surface expands outward. An image showing the overheated conditions is depicted in Figure S4 (b). When the volume energy density  $E_v$  is reduced to a range  $28\text{ J mm}^{-3} < E_v < 44\text{ J mm}^{-3}$ , the molten pool shows fluctuations that are ascribed mainly to the laser scanning speed at both the beginning and end points of a scanning track where the laser dwells longer over the powder bed and more laser energy is absorbed than in the middle of the track. The overheated molten pool at the edges tends to flow towards the middle region, resulting in strong melt convection that distorts the forming layer. At volume energy densities  $E_v$  in the range from  $10\text{ J mm}^{-3}$  to  $28\text{ J mm}^{-3}$ , the powder bed absorbs just the right amount of energy to melt the powder and the interface between the powder bed and substrate so that they can tightly fuse together, producing a flat and dense forming layer. At volume energy densities  $E_v$  held between  $4\text{ J mm}^{-3}$  and  $10\text{ J mm}^{-3}$ , which corresponds to the granular image in Figure S4 (b), there is not enough energy to melt the powder bed through, and the relatively low temperature and high viscosity of the molten pool increases the wetting angle between the molten pool and substrate, giving rise to a balling phenomenon. At volume energy densities  $E_v$  below  $4\text{ J mm}^{-3}$ , the absorbed energy is entirely insufficient to melt most of the powder bed except at the start and end points of the laser track. Consequently, the powder in the middle of the powder bed gets separated from the substrate and an unattached forming layer result. One should note that the hatch spacing  $h = 0.05\text{ mm}$  and the dried powder bed thickness  $d = 30\text{ mm}$  were fixed and once either one is altered, the above process window will change accordingly.

From the above results it follows that to form a high-quality forming thin layer, the laser energy density and the scanning speed are the critical parameters that have to be carefully controlled. Identifying and maintaining the optimal processing parameters is the key prerequisite to making the printing process *via* the SLM technology a successful undertaking. Considering the quality and characteristics of the forming layer, the identified parameters of  $P = 7 \text{ W}$ ,  $v = 200 \text{ mm/s}$ ,  $h = 0.05 \text{ mm}$  and  $d = 30 \text{ mm}$  were used in the process of printing bulk materials in this paper.

## Volatilization characteristics



**Figure S5.** (a) Temperature profile during the SLM process; (b)-(c) The calculated vaporization rates and saturated vapor pressures as a function of the molten pool's temperature for printing a solid solution with composition  $\text{Bi}_{0.4}\text{Sb}_{1.6}\text{Te}_3$ .

Figure S5 (a) gives the temperature variation as a function of time during the SLM process. The temperature rises sharply to more than 2000 K in less 0.005 s, and rapidly drops to room temperature in fewer than 0.05 s. The maximum temperature far exceeded the melting point of the p-type BiSbTe material, and reached even higher than its boiling point. According to the kinetic theory of alloy elemental volatilization, the vaporization rate  $J_i$  ( $\text{g}\cdot\text{cm}^{-2}\cdot\text{s}^{-1}$ ) of an element  $i$  in the molten pool of an alloy is given by the Langmuir equation<sup>2</sup>:

$$J_i = 4.375 \times 10^{-4} \gamma_i X_i P_i^0 \left( \frac{M_i}{T} \right)^{1/2} \quad (2)$$

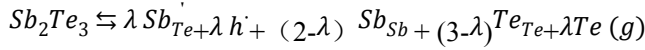
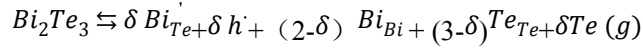
where  $\gamma_i$  is the active coefficient of element  $i$ ,  $X_i$  is its molar fraction,  $P_i^0$  is the vapor pressure of pure element  $i$  (Pa),  $M_i$  is its atomic weight ( $\text{g}\cdot\text{mol}^{-1}$ ), and  $T$  (K) is the temperature of the molten pool. The vapor pressure can be calculated from the following equation<sup>3</sup>:

$$\log P_i^0 = -\frac{A}{T} + B + C \log T \quad (3)$$

where  $A$ ,  $B$  and  $C$  are the related constants. Substituting equation (3) into (2), the vaporization rate of each element at different temperatures can be readily acquired. As illustrated in Figures S5 (b)-(c), both the  $J_i$  and  $P_i^0$  of Bi and Sb are almost unchanged as the temperature increases, indicating that Bi and Sb will not be lost due to volatilization during the rapid heating processing. For Te, on the other hand, the  $J_i$  and  $P_i^0$  increase slowly with the rising temperature of the molten pool up to 1400 K, and then a steep increase sets in at higher temperatures, which likely results in a significant

loss of Te to volatilization during the SLM process. It is well-known that the loss of Te will lead to the formation of anti-site defects  $Bi_{Te}'$  and  $Sb_{Te}'$  on account of comparable atomic radii and electronegativities of Bi/Sb and Te. This would increase the hole carrier concentration and vastly degrade the thermoelectric properties, as illustrated by the following defect equations:

Centralized  
alignment



Right  
alignment

Assuming a single parabolic band model, the relationship between the carrier concentration and the Seebeck coefficient is expressed as<sup>4</sup>:

$$S = \frac{8\pi^2 \kappa_B^2}{3eh^2} m^* T \left(\frac{\pi}{3p}\right)^{2/3} \quad (6)$$

Here,  $\kappa_B$ ,  $h$ ,  $e$ ,  $S$ ,  $m^*$  and  $p$  are the Boltzmann constant, the Planck constant, the charge of an electron, the Seebeck coefficient, the carrier effective mass and the hole carrier concentration, respectively. Obviously, as follows from equation (6), the Seebeck coefficient is negatively correlated with the carrier concentration of holes. Therefore, some measures must be adopted, such as composition compensation, to suppress the formation of anti-site defects during the SLM process as much as possible.

## Composition compensation

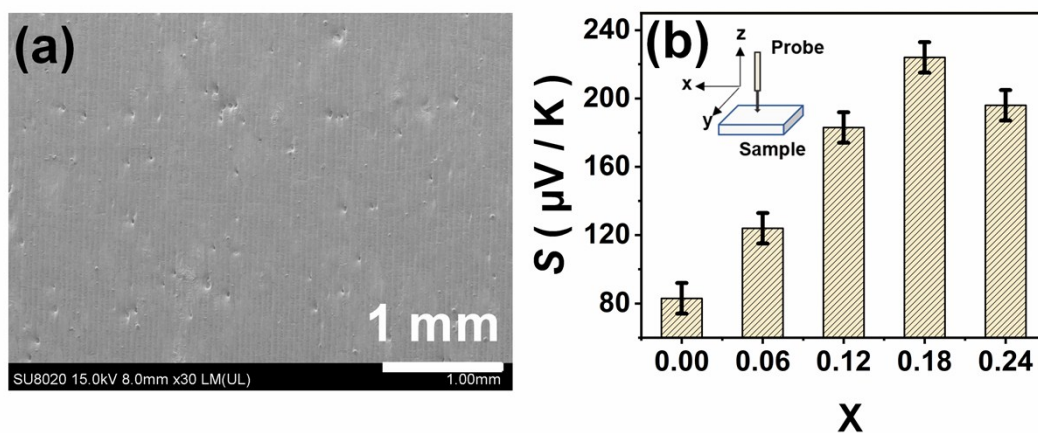


**Figure S6.** (a) A representative FESEM image of surface morphology of the forming layers of  $\text{Bi}_{0.4}\text{Sb}_{1.6}\text{Te}_{3+x}$  ( $x = 0, 0.06, 0.12, 0.18, 0.24$ ) samples; (b) the average Seebeck coefficient of the  $\text{Bi}_{0.4}\text{Sb}_{1.6}\text{Te}_{3+x}$  forming layers with different Te compensation contents  $x$ . The inset is a schematic diagram of the PSM test principle.

As stated above, to inhibit the forming of anti-site defects in the SLM process as much as possible, the composition compensation experiment was carried out by adding an excess amount of Te to a powder processed by thermal explosion. A series of powders with the nominal compositions  $\text{Bi}_{0.4}\text{Sb}_{1.6}\text{Te}_{3+x}$  ( $x = 0, 0.06, 0.12, 0.18, 0.24$ ) were prepared and the average Seebeck coefficient was used to assess the optimal Te content. First of all, three thin-layers with different  $x$  were printed under the same processing conditions; then the surface average Seebeck coefficient of different samples was measured by PSM. The scanning area was  $4 \times 4 \text{ mm}^2$ , and both the horizontal and longitudinal step lengths were  $50 \mu\text{m}$ , 6400 points in total. Figure S6 (a) is a representative FESEM image of surface morphology of the forming layer of  $\text{Bi}_{0.4}\text{Sb}_{1.6}\text{Te}_{3+x}$  samples. Figure S6 (b) shows the average Seebeck coefficient of the forming layers compensated with different Te contents. The average Seebeck coefficient of the sample without any Te compensation is just  $82 \mu\text{V}/\text{K}$ , but increases with the increasing  $x$  and reaches the peak value of  $225 \mu\text{V}/\text{K}$  for  $x = 0.18$ . With a further increase beyond  $x = 0.18$ , the Seebeck coefficient tends to decrease. This is ascribed to an excessive amount of Te beyond the optimal value, which would then act as a donor dopant by occupying the cation positions of Bi/Sb, leading to an increased concentration of minority carriers and the ensuing degradation

of the Seebeck coefficient. The above results demonstrate that anti-site defects could be inhibited by a judiciously chosen over stoichiometry of Te in the initial powder mixture. According to the experimental results,  $\text{Bi}_{0.4}\text{Sb}_{1.6}\text{Te}_{3.18}$  was chosen as the nominal composition for the preparation of p-type BiSbTe precursor powders used in the SLM printing process.

## Microstructure of as-printed sample

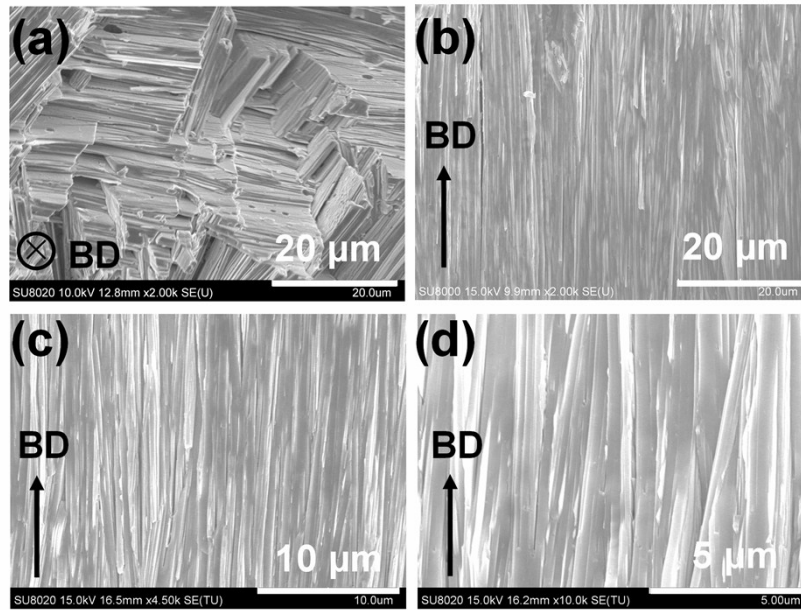


**Figure S7.** SEM images of (a) disordered grains of the plane perpendicular to the building direction and (b)-(d) oriented column-like grains of the plane parallel to the building direction in different magnifications.

## Relationship between grain orientation and XRD result

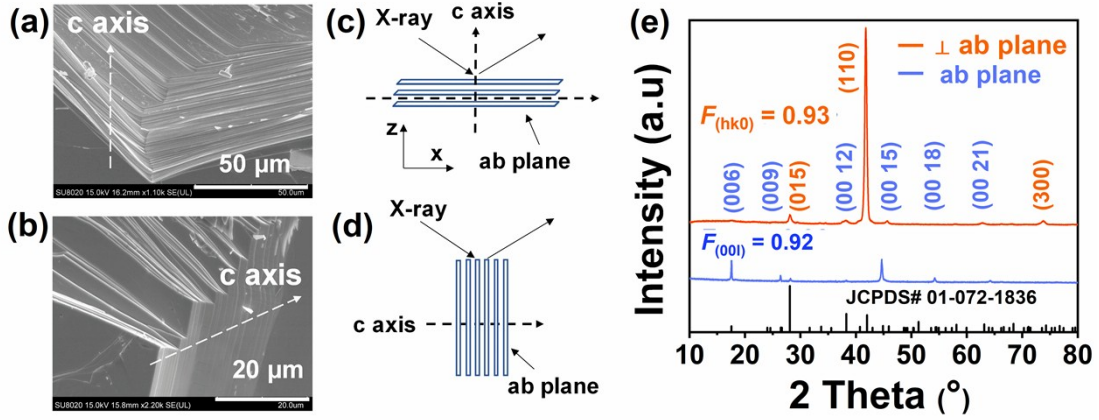


**Figure S8.** (a)-(b) SEM images of the morphology of different planes of the ZM p-type BiSbTe single crystal; (c)-(d) Spatial relationship between the grain orientation and XRD-scanned planes; (e) XRD patterns of the ab plane and a plane perpendicular to the ab plane of the ZM p-type BiSbTe single crystal.

The crystallographic orientation of Bi<sub>2</sub>Te<sub>3</sub>-based materials has a significant influence on the TE and mechanical properties of the materials. The orientation (or the degree of texture) is conventionally evaluated by introducing the orientation factor  $F$  along the crystallographic c-axis ([00 $l$ ] direction) defined as

$$F = \frac{P - P_0}{1 - P_0} \quad (7)$$

$$P_0 = \frac{\sum I_0(00l)}{\sum I_0(hkl)} \quad (8)$$

$$P = \frac{\sum I(00l)}{\sum I(hkl)} \quad (9)$$

Right alignment

Here,  $I(hkl)$  and  $I(00l)$  are intensities of the  $(hkl)$  and  $I(00l)$  diffraction peaks of the printed bulk sample, respectively, and  $I_0(hkl)$  and  $I_0(00l)$  are intensities of the  $(hkl)$  and  $I_0(00l)$  diffraction peaks of the powdered specimens, respectively. A sample has no preferred orientation when the orientation factor  $F$  equals 0, just like the powder sample, and it is fully-oriented when the orientation factor  $F$  equals 1, such as a high-quality single crystal sample. The larger the  $F$  value, the stronger the grain orientation in the material<sup>5, 6</sup>. The traditional calculation equations are based on the (00 $l$ ) plane, according to the Bragg

diffraction law, however, the surface on which the XRD measurement is done should be consistent with the (00*l*) lattice plane, shown in Figure S8 (c). Provided the (00*l*) plane is perpendicular to the measurement surface, shown in Figure S8 (d), (*hk*0) diffraction peaks would dominating in the XRD pattern. In this case, the (00*l*) plane in equations (7)-(9) should be replaced by the following equations:

$$F = \frac{P - P_0}{1 - P_0} \quad (10)$$

$$P_0 = \frac{\sum I_0(hk0)}{\sum I_0(hkl)} \quad (11)$$

$$P = \frac{\sum I(hk0)}{\sum I(hkl)} \quad (12)$$

**Right  
alignment**

XRD patterns of (00*l*) and (*hk*0) planes of the p-type BiSbTe single crystal prepared by ZM are presented in Figure S8 (e). The pattern shows that the p-type BiSbTe single crystal by the ZM sample have a strong orientation. The preferential orientations *F* of the (00*l*) and (*hk*0), calculated by equations (7)-(9) and (10)-(12), are 0.92 and 0.93, respectively, showing almost the same value.

### XRD patterns and microstructure of annealed sample

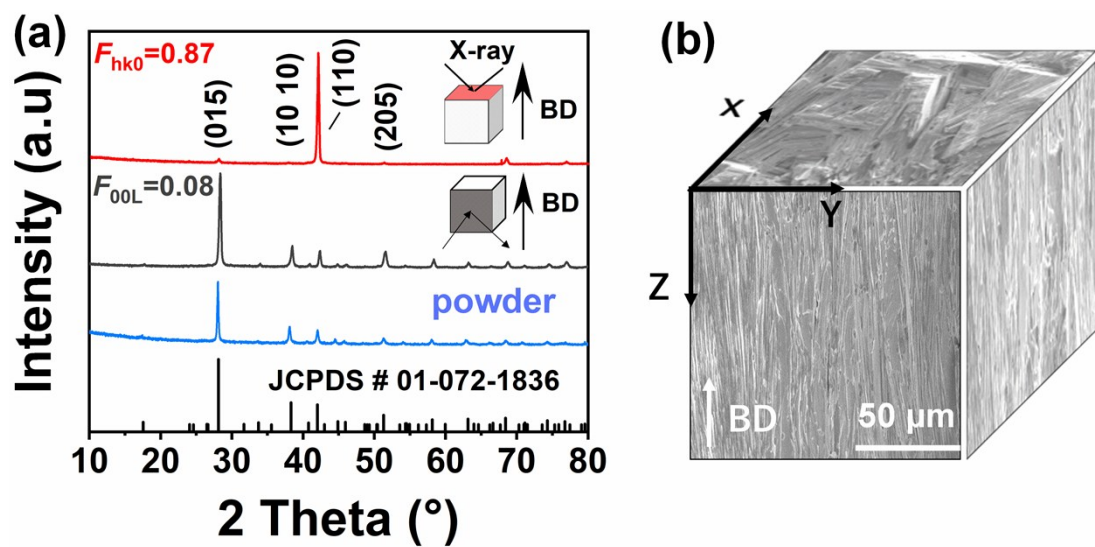


**Figure S9.** (a) XRD patterns of planes perpendicular and parallel to the building direction (BD), and of the ground powder of the annealed bulk material; (b) grain morphologies of cross section planes XY, XZ, YZ of the sample after annealing.

### Microstructure of annealed sample (TEM)

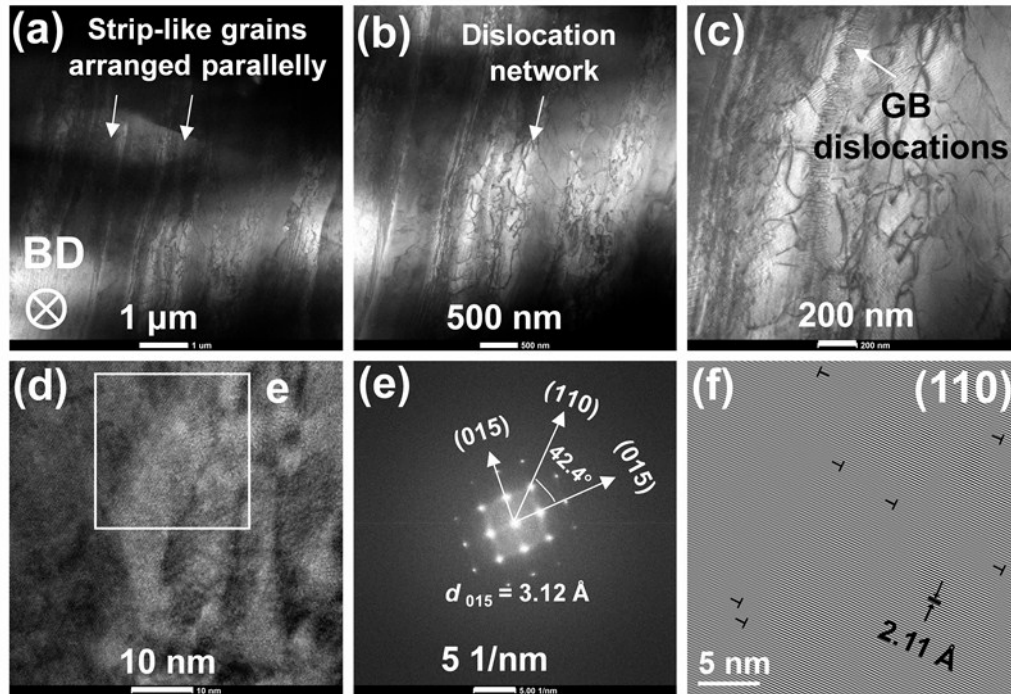


**Figure S10.** TEM images of (a) a cross section perpendicular to the building direction, showing the parallel array of strip-like grains. (b) Irregular arrangement of dislocation networks within the grains. (c) Parallel dislocation lines at grain boundaries (GB). (d) HRTEM image of irregular dislocations within the grain. (e) SAED image of the white-boxed region in (d). (f) IFFT image of the (110) plane, showing high density of dislocation and lattice distortions within the light grey regions.

## Uniformity of TE properties of annealed samples

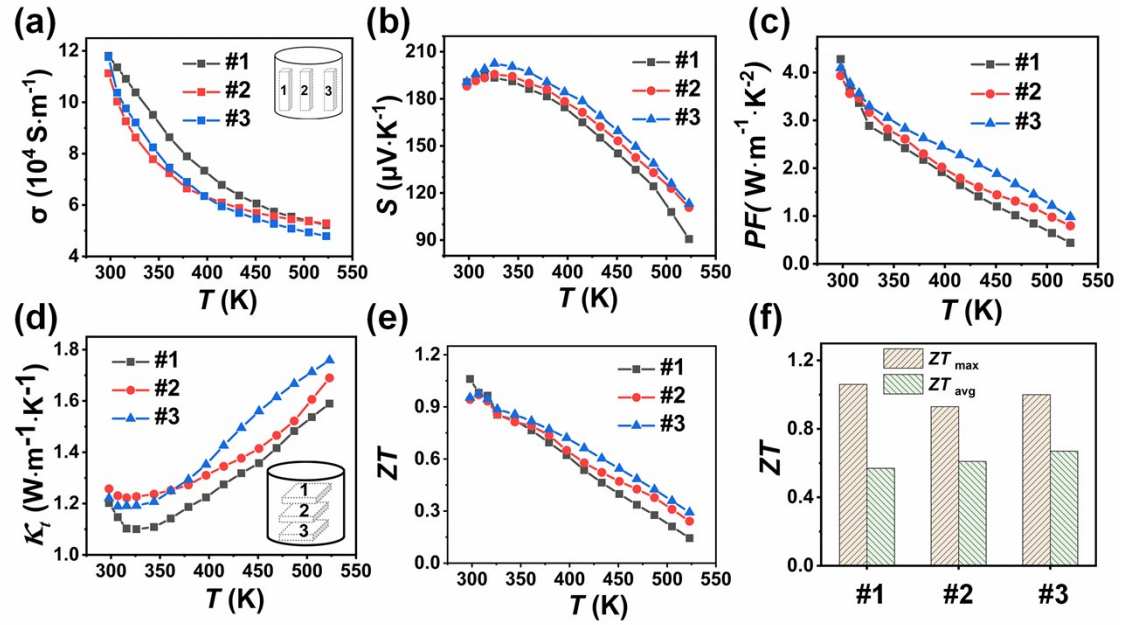


**Figure S11.** Uniformity of thermoelectric properties of a big sample after annealing. Both electronic and thermal properties were measured along the building direction. Temperature dependence of (a) the electrical conductivity, (b) the Seebeck coefficient, (c) the power factor, (d) the total thermal conductivity, and (e) the figure-of-merit  $ZT$ . (f) A comparison of the maximum and average  $ZT$  values of the three samples in the temperature range 300 K-525 K. Samples #1, #2, and #3 are taken from printed bulk at locations marked in insets in Figs. S11(a) and S11(d).

## Stability of TE parameters of the annealed sample

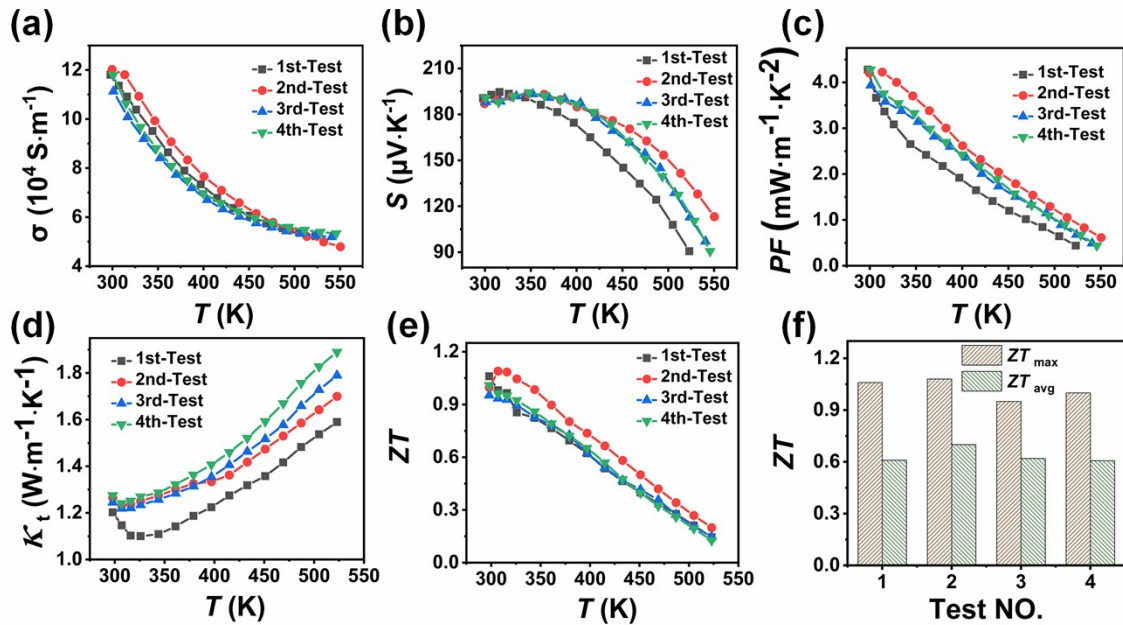


**Figure S12.** Stability of thermoelectric parameters after up to four cycles of measurements to a temperature of 525 K. Measurements taken on a sample oriented along the building direction. Temperature dependence of (a) the electrical conductivity, (b) the Seebeck coefficient, (c) the power factor, (d) the total thermal conductivity, and (e) the figure-of-merit  $ZT$ . (f) A comparison of the maximum and average  $ZT$  values for the SLM-printed sample measured in the range of 300 K–525 K.

## References

1. L. Thijs, F. Verhaeghe, T. Craeghs, J. V. Humbeeck and J.-P. Kruth, *Acta Materialia*, 2010, **58**, 3303–3312.
2. A. Block-Bolten and T. W. Eagar, *Metallurgical Transactions B*, 1984, **15**, 461–469.
3. E. A. Brandes and G. B. Brook, *Smithells Light Metals Handbook*, 1998, **20**, 163 – 172.
4. G. J. Snyder and E. S. Toberer, *Nature Materials*, 2008, **7**, 105–114.
5. M. Kroutvar, Y. Ducommun, D. Heiss, M. Bichler, D. Schuh, G. Abstreiter and J. J. Finley, *Nature*, 2004, **432**, 81–84.
6. G. Zheng, X. Su, H. Xie, Y. Shu, T. Liang, X. She, W. Liu, Y. Yan, Q. Zhang, C. Uher, M. G. Kanatzidis and X. Tang, *Energy & Environmental Science*, 2017, **10**, 2638–2652.

**Please remove the blank page**